# Chapter 4

# The disk billiard

*The disk billiard in homogeneous magnetic fields is used as a model system for semiclassical approximations. Its quantum mechanical level density can be calculated analytically. Therefore, a precise comparison of the semiclassical approach to the exact result is possible. The influence of various $\hbar$-corrections to the trace formula is examined. With the help of the trace formula's close relation to classical dynamics it is possible to give a simple, intuitive picture explaining all features of the level density.*

## Contents

The trace formula is a relatively new technique in mesoscopic physics. The experience with the approach is therefore rather limited. The application of this method to a simple, well-known model system has three motivations: First, it is desirable to test the new ansatz on a non-trivial, but well-known reference system to learn about the limitations of the method. So the second goal considering a model system is to find out under which circumstances specific corrections in higher order of $\hbar$ become relevant. Finally, in cases where these corrections are not negligible, the challenge is to improve the semiclassical ansatz, i.e. to include the relevant corrections in a generalized trace formula.

The semiclassical description of the disk billiard in homogeneous magnetic fields is therefore worked out not *although* the problem can be solved exactly, but *because* it can. The three goals formulated above will serve as a guiding line through the following sections.

## 4.1 Exact quantum solution

The disk billiard in homogeneous magnetic fields is integrable. The two constants of motion are the angular momentum and the energy. In the following, normalized energies $\widetilde{E}$ in units of

$$E_0 = \frac{\hbar^2}{2mR^2} \tag{4.1}$$

and normalized magnetic fields $\widetilde{B}$ in units of $\hbar/eR^2$ will be used. With the disk radius $R$ and the wavenumber $k$ the normalized energy is given by $\sqrt{\widetilde{E}} = kR$. The classical cyclotron radius is given by $R_c = \hbar k/eB$, and in normalized units by $R_c/R = kR/\widetilde{B}$. The exact solution for the eigenenergies was presented by Geerinckx [31] and, using a different approach, by Klama *et al.* [49]:

$$\widetilde{E}_{nl} = 2\widetilde{B} \cdot \left( \alpha_{nl} + \frac{1+|l|}{2} + \frac{1}{2} \right) \ , \tag{4.2}$$

where the $\alpha_{nl}$ are the zeros of the confluent hypergeometric function ${}_1F_1$

$${}_1F_1\left( -\alpha_{nl}; 1+|l|; \frac{\widetilde{B}}{2} \right) = 0 \ . \tag{4.3}$$

Here $n > 0$ denotes the radial and $l$ the angular-momentum quantum number. For $B = 0$ the eigenvalue equation simplifies to the well-known result $\widetilde{E}_{nl} = (j_{nl})^2$, where $j_{nl}$ are the zeros of the Bessel functions $J_l(j_{nl}) = 0$. For the details of the numerical evaluation, I refer to my Diploma thesis [1]. Fig. 4.1 shows the dependence of the eigenvalues $\widetilde{E}_{nl}$ on $\widetilde{B}$. One clearly sees how with increasing magnetic field the different states condense into the Landau levels (dashed lines).

## 4.2 The leading order in $\hbar$: Standard semiclassics

The standard Gutzwiller approach [36, 37, 38, 39, 40] is limited to orbits which are isolated in phase space. Therefore it cannot be applied to the disk with its continuous rotational

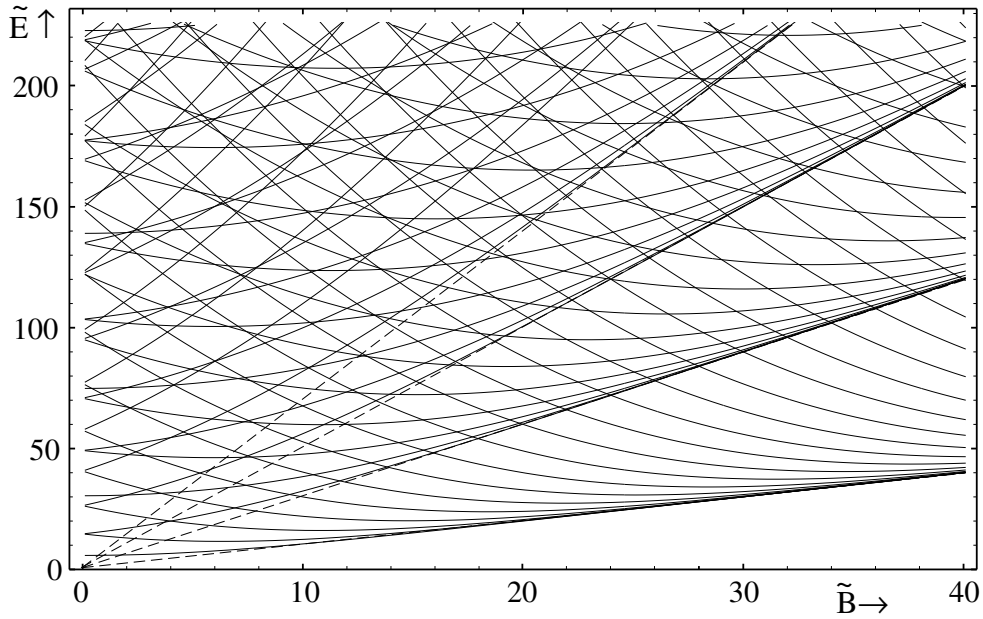


Figure 4.1: *The quantum-mechanical eigenenergies of the circular billiard in dependence of the magnetic field. The dashed lines correspond to the four lowest Landau levels.*

symmetry. Deriving a trace formula requires the extensions of Strutinisky and Magner [76] or Creagh and Littlejohn [23]. This has been done for the zero-field case by Reimann *et al.* [2] and, independently, by Tatievski *et al.* [79]. Equivalent results have been obtained by Balian and Bloch [11]. Von Oppen [123] followed the approach of Berry and Tabor [13], which starts from the EBK quantization of the system [46]. Via Poisson resummation and subsequent saddle point approximations he derived a trace formula equivalent to the modified Gutzwiller approach. This result shows that EBK and the modified Gutzwiller approximation are identical in the leading order of $\hbar$. Since the intermediate steps of the calculation include saddle-point approximations, the identity does not necessarily hold beyond the leading order. In a previous work I was, however, able to show numerically with high accuracy that the Gutzwiller-like trace formula reproduces exactly[1] the single-particle energies of the EBK quantization. For details see Refs. [2, 1].

For weak magnetic fields, the circular billiard was treated using a perturbative approach by Bogachek and Gogadze [15], Ullmo *et al.* [82] and Reimann *et al.* [62].

### 4.2.1 Trace formula for arbitrarily strong fields

The generalization of the Gutzwiller trace formula to systems with continuous symmetries by Creagh and Littlejohn is a convenient starting point for the semiclassical description of the level density of a circular billiard in arbitrarily strong magnetic fields. For the application of this generalized trace formula, the periodic orbits have to be classified and their actions, amplitudes, and Maslov indices have to be calculated. This was the topic of my diploma thesis [1]. Since these results provide the basis for the subsequent calculations, they will be shortly reviewed in the following.

[1] This has to be interpreted as a very fortunate case, comparable to the harmonic oscillator. There all $\hbar$ corrections vanish, and the semiclassical approximation is therefore exact [18].

#### 4.2.1.1 Classification of the periodic orbits

The classification of the periodic orbits in the system is straightforward. In zero field, the periodic orbits (PO) of a circular billiard are equivalent to those in a three-dimensional spherical cavity. The complete classification of those has already been given by Balian and Bloch [11]. The only difference to the three-dimensional case is that the orbits in the disk billiard only have a one-dimensional degeneracy, corresponding to the rotational symmetry of the system. Each family of degenerate orbits with a given action can be represented by a regular polygon. The first few polygons are shown in Fig. 4.2. These

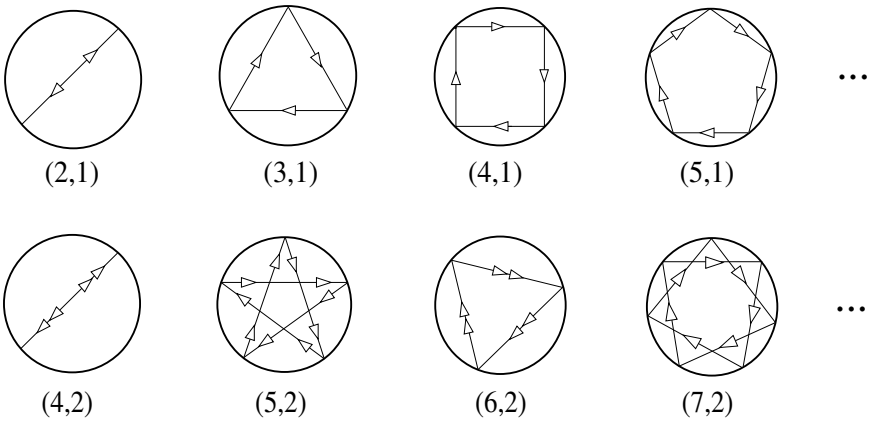


Figure 4.2: *The classical periodic orbits of the circular billiard in zero field are the regular polygons. They can be classified with $(v, w)$, where $v$ is the number of corners and $w$ indicates how often the trajectory winds around the center.*

orbit families are classified by $\beta = (v, w)$, where $v$ denotes the number of corners (vertices), and $w$ is the winding number, i. e., it counts how often an orbit winds around the center of the disk. With $v \geq 2w > 2$ $(v, w \in \mathbb{N})$, all families of POs of the system in the absence of a magnetic field are uniquely described by $\beta = (v, w)$. Because of the time-reversal symmetry, all orbits except the diameter $(v = 2w)$ have an additional discrete two-fold degeneracy, which has to be accounted for in the trace formula.

Switching on the magnetic field causes the classical trajectories to bend, the direction of the curvature depending on the direction of motion with respect to the magnetic field. This entails a breaking of time-reversal symmetry. For weak fields, the orbits can still be classified by $\beta$ if an additional index $(\pm)$ is introduced. This situation is shown in the upper row of diagrams in Fig. 4.3 for the orbit $\beta = (4, 1)$. Up to a field strength where the

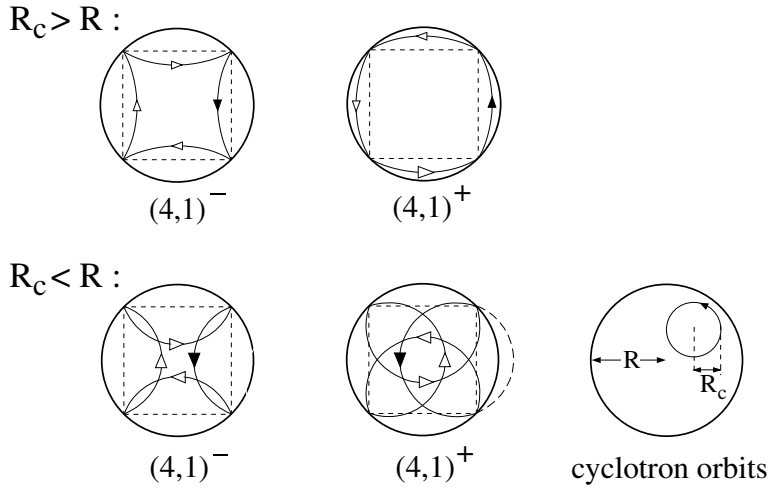


Figure 4.3: *A magnetic field breaks the time-reversal symmetry, so that the orbits are no longer independent of the direction of motion. Introducing an additional index $\pm$, the orbits can be classified by $(v, w)^{\pm}$, both in weak $(R_c > R)$ and in strong $(R_c < R)$ fields. For strong fields an additional family of orbits occurs. These are the cyclotron orbits, which do not touch the boundary.*

classical cyclotron radius $R_c$ equals the disk radius $R$, henceforth referred to as the *weak-field regime*, the orbits do not change their topology and the classification $\beta^{\pm}$ holds. For the *strong-field regime* with $\widetilde{B} > kR$, the structure of the POs is different. This situation is shown in the second row of diagrams in Fig. 4.3. The $\beta^-$ orbits vary their shapes continuously over the point $R_c = R$, but the topologies of the $\beta^+$ orbits change abruptly. However, since there is a one-to-one correspondence between orbits for $R_c \gtrsim R$ and for $R_c \lesssim R$, $\beta^{\pm}$ still gives a complete classification of all *bouncing orbits*, i. e., of orbits that are reflected at the boundary. For $R_c < R$, there are additional *cyclotron orbits* which do not touch the boundary at all. They have to be included additionally in the sum over all orbits in the trace formula. At field strengths where $R_c \leq R \cdot \sin(\pi w/v)$, the $(v,w)^{\pm}$ orbits no longer exist (see Fig. 4.4). They vanish pairwise in a tangent bifurcations. This imposes

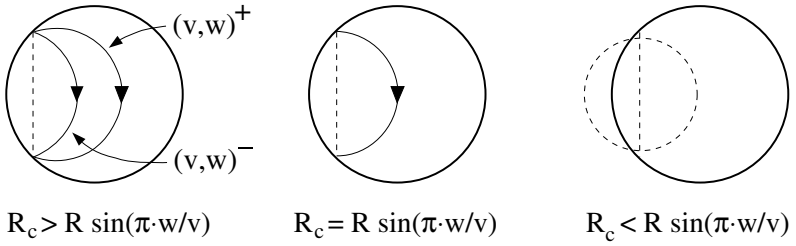


Figure 4.4: *At a magnetic field strength where $R_c = R\sin(\pi\ w/v)$, the orbits $(v,w)^{\pm}$ vanish pairwise in tangent bifurcations.*

an additional restriction on the sum over $(v,w)$. Including this finally yields a complete classification of all periodic orbits in the circular billiard at arbitrary field strengths.

#### 4.2.1.2 The bouncing orbits

The action of a closed orbit in a magnetic field can be written as the sum of the kinetic part and the magnetic flux enclosed by the orbit

$$S_\beta = \int p\,\mathrm{d}q = \hbar k L_\beta - eBF_\beta\,. \tag{4.4}$$

The enclosed areas $F_\beta$ of the periodic orbits discussed above (correctly counting those areas that are enclosed several times, cf. Fig. 4.5) as well as their geometrical lengths $L_\beta$

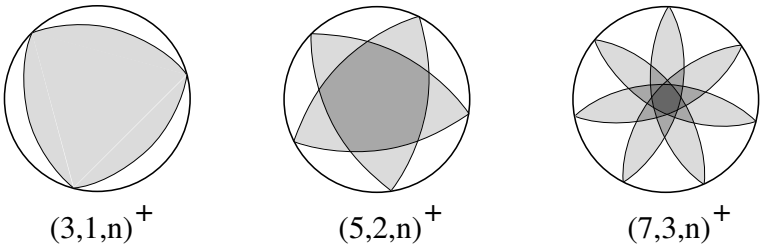


Figure 4.5: *Calculating the magnetic flux enclosed by an orbit, the multiple enclosed areas (darker gray) have to be correctly accounted for.*

can be calculated by elementary geometry. In terms of the geometrical quantities $R_c, R, \gamma$ and $\Theta$ explained in Fig. 4.6 they are given by

$$S_\beta(E) \;=\; v\hbar k R_c \eta\,, \tag{4.5}$$

$$\eta = \begin{cases} \gamma + \frac{\sin 2\gamma}{2} - \left(\frac{R}{R_c}\right)^2 \frac{\sin 2\Theta}{2} & \text{for } (\beta^+, R_c \geq R) \\ \pi - \gamma - \frac{\sin 2\gamma}{2} + \left(\frac{R}{R_c}\right)^2 \frac{\sin 2\Theta}{2} & \text{for } (\beta^+, R_c \leq R) \\ \gamma + \frac{\sin 2\gamma}{2} + \left(\frac{R}{R_c}\right)^2 \frac{\sin 2\Theta}{2} & \text{for } (\beta^-) \end{cases} .$$

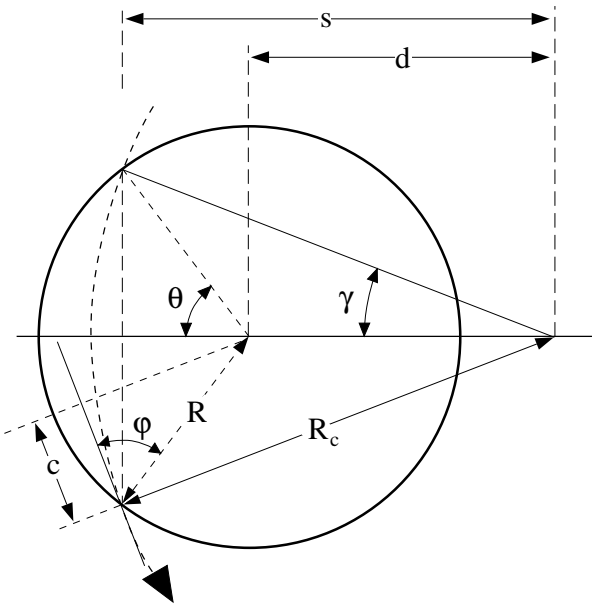


Figure 4.6: *The actions and amplitudes of the classical periodical orbits can be expressed in terms of the geometrical quantities shown in this figure.*

According to the trace formula Eq. (2.15), the orbit amplitudes include an integral over the symmetry group. For the rotational $U(1)$ symmetry of the disk this integral just gives $2\pi/v$. The remaining factors in the amplitude are the period of the orbit $L/\hbar k$, and the Jacobian resulting from the symmetry reduction $\mathrm{d}L/\mathrm{d}\Psi$, where $\Psi = -2n\Theta$. All these quantities can be calculated analytically, resulting in

$$\begin{aligned} A_\beta &= \frac{1}{E_0} \frac{1}{\sqrt{Rk\pi}} \frac{1}{\sqrt{v}} \frac{R_c}{R} \sqrt{\frac{cd}{sR}}\, \xi_\beta , \\ \xi_\beta &= \begin{cases} \pi - \gamma & \text{for } (\beta^+, R_c < R) \\ \gamma & \text{otherwise} \end{cases} , \end{aligned} \tag{4.6}$$

where $c, d$, and $s$ are the geometrical lengths sketched in Fig. 4.6. The dependence of these geometrical quantities on the classification parameter $\beta^\pm$ and the cyclotron radius $R_c$ is given by

$$\begin{aligned} \Theta &= \frac{w}{v}\pi , \\ \gamma &= \arcsin\left(\frac{R}{R_c}\sin\Theta\right) , \\ \varphi &= \begin{cases} \gamma - \Theta + \pi/2 & \text{for } (\beta^+, R_c > R) \\ -\gamma + \Theta + \pi/2 & \text{for } (\beta^+, R_c < R) \\ \gamma + \Theta - \pi/2 & \text{for } (\beta^-) \end{cases} , \\ c &= R\cos\varphi , \\ s &= \sqrt{{R_c}^2 - R^2\sin^2\Theta} , \\ d &= \begin{cases} |s - R\cos\Theta| & \text{for } \beta^+ \\ s + R\cos\Theta & \text{for } \beta^- . \end{cases} \end{aligned} \tag{4.7}$$

#### 4.2.1.3 Cyclotron orbits

As already mentioned above, a new class of orbits occurs for $\widetilde{B} > kR$. These are the *cyclotron orbits*, which do not touch the boundary at all (see Fig. 4.3). They form translationally degenerate families, whereas the bouncing orbits $(v, w)^\pm$ considered above are

degenerate with respect to rotations. For the translational case, the symmetry reduction can be performed directly, without need for the general procedure of Creagh and Littlejohn. Therefore, the the phase-space coordinates are transformed according to

$$\pi_x := \frac{1}{\sqrt{|eB|}}\left(p_x + \frac{eB}{2}y\right) , \qquad \Pi_x := \pi_y + \sqrt{|eB|}\, x ,$$
$$\pi_y := \frac{1}{\sqrt{|eB|}}\left(p_y - \frac{eB}{2}x\right) , \qquad \Pi_y := \pi_x - \sqrt{|eB|}\, y . \tag{4.8}$$

$\Pi_x$ and $\Pi_y$ are canonically conjugate variables, since $[\Pi_x, \Pi_y] = i\hbar$. The same holds for $\pi_x$ and $\pi_y$. Apart from the factor $\sqrt{|eB|}$, $(\pi_x, \pi_y)$ are the coordinates of the motion relative to the center of gyration $(\Pi_x, \Pi_y)$, as illustrated in Fig. 4.7. In these coordinates the Hamiltonian reads

$$H = \frac{eB}{2m}(\pi_x^2 + \pi_y^2) . \tag{4.9}$$

As expected, $H$ does not depend on the coordinates of the center of gyration. Because the relative and the center-of-gyration coordinates commute, i. e., $[\Pi_x, \pi_x] = [\Pi_x, \pi_y] = [\Pi_y, \pi_x] = [\Pi_y, \pi_y] = 0$, the degeneracy of a cyclotron orbit is proportional to the phase-space volume $V$ accessible for $(\Pi_x, \Pi_y)$. This can be directly read off Fig. 4.7 (shaded area). The degeneracy is therefore given by

$$N = \frac{V}{2\pi\hbar} = \frac{\tilde{B}}{2}\left(1 - \frac{R_c}{R}\right)^2 . \tag{4.10}$$

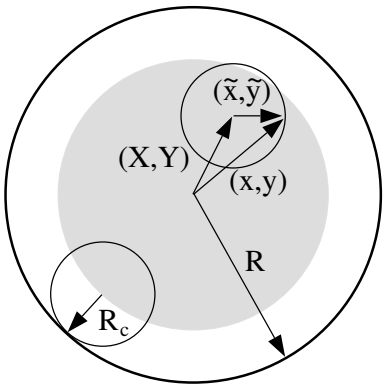


Figure 4.7: *The motion of a charged particle in a homogeneous magnetic field can be expressed in the coordinates of the relative motion* $(\tilde{x}, \tilde{y}) = |eB|^{-1/2}(-\pi_y, \pi_x)$ *and the coordinates of the center of gyration* $(X, Y) = |eB|^{-1/2}(\Pi_x, -\Pi_y)$. *The Hamiltonian is independent of* $(\Pi_x, \Pi_y)$*; all orbits with the center* $(X, Y)$ *in the gray shaded area are degenerate.*

The Hamiltonian Eq. (4.9) is identical to that of a one-dimensional harmonic oscillator. Using its analytical trace formula,[2] the contribution of the cyclotron orbits to the oscillating part of the level density can be written as

$$\delta g^c = \frac{1}{2E_0}\left(1 - \frac{R_c}{R}\right)^2 \sum_{n=1}^{\infty} \cos(nk\pi R_c - n\pi) . \tag{4.11}$$

Here $n$ is the winding number around the center of gyration. The frequency is again determined by the classical action along the orbit, which in this case is

$$S = n \cdot \hbar k \cdot \pi R_c . \tag{4.12}$$

Note that here exactly half of the kinetic contribution to the action is canceled by the flux term.

[2] The one dimensional harmonic oscillator is one of the few cases that can be treated exactly within standard POT [18].

#### 4.2.1.4 Additional phases

The additional phases $\sigma$ in the trace formula (2.15) are discussed in Sec. 4.3.2.1. There, the Maslov index $\mu$ is found to be $\mu = 3v$ for bouncing orbits and $\mu = 2$ for cyclotron orbits. The additional phase of $\delta \cdot \pi/2$ stemming from the symmetry reduction is given by

$$\delta = \begin{cases} 0 & \text{for } (\beta^+, R_c < R) \\ 1 & \text{otherwise} \end{cases} . \tag{4.13}$$

Now for all quantities of the trace formula analytical expressions have been derived. Inserting them in Eq. (2.15), the semiclassical level density for the disk billiard in homogeneous magnetic fields can be evaluated.

### 4.2.2 Numerical evaluation

The infinite trace sum Eq. 2.15 has to be truncated in a numerical evaluation. The implications of this truncation have been discussed in Sec. 3.4. To ensure the convergence of the sum and the comparability with the quantum results as well as to control the truncation errors, the considerations of Sec. 3.2 will now be applied to the trace formula of the disk billiard.

As discussed on page 20, the natural choice for the generalized energy in billiard systems is $k$. According to Eq. (3.21) the quasiperiod is then given by the geometrical orbit length

$$L = vR_c \cdot \begin{cases} 2\pi - 2\gamma & \text{for } (\beta^+, R_c < R) \\ 2\gamma & \text{otherwise} \end{cases} . \tag{4.14}$$

Note that for weak fields ($R_c > R$) $L$ is independent of the direction of motion $\pm$.

To compute the trace formula, an appropriate window function $F(L)$ has to be selected. For this choice two criteria are relevant: First, $F(L)$ should be nonzero only in a finite range of $L$, so that many terms in the trace formula are eliminated and the numerical evaluation is simplified. Second, the window function should have an analytical Fourier transform to enable an easy and accurate comparison with the quantum results. Either of these conditions is met by the usual Gaussian smoothing, where the orbits are suppressed with increasing length $L$ according to $\exp\{-(L/L_0)^2\}$. In this work a triangular window is used instead, which matches both demands. In order to make the results comparable with the usual Gaussian smoothing, the window function is characterized with a parameter $\tilde{\gamma}$. It corresponds to the variance of a Gaussian smoothing $\exp\{-1/2(k/\tilde{\gamma})^2\}$ with the same half-width.

Since the trace formula should be evaluated via Eq. (3.14), the compliance of conditions Eqs. (3.19) and (3.20) has to be checked. These depend on the behavior of the amplitudes which are plotted in Fig. 4.18. As already discussed, the orbit amplitudes diverge at the bifurcations, so that Eq. (3.20) is violated at these points. This problem will be treated together with the inclusion of the bifurcations in Sec. 4.3.3. Except in the vicinity of bifurcations, the conditions (3.19) and (3.20) are fulfilled, so that Eq. (3.14) is applicable. For the cyclotron orbits discussed in Sec. 4.2.1.3, $G = n \cdot 2\pi R_c$ and $A = (2E_0)^{-1}(1-R_c/R)^2$. This amplitude is slowly varying in the whole energy range. For the cyclotron orbits, approximation (3.18) is therefore justified for all $\widetilde{E}$ and $\widetilde{B}$.

Putting everything together, this establishes a numerical scheme for the evaluation of the semiclassical trace formula for the circular billiard.

### 4.2.3 Results of the trace formula

The results of the trace formula for the disk billiard in homogeneous magnetic fields will only be discussed insofar as they are relevant for the present work. Further details can be found in my Diploma thesis [1] or in Ref. [4].

For zero field, the trace formula leads to an exact quantization at the EBK eigenvalues [2]. In the weak-field limit the trace formula can be approximated by replacing the amplitudes of Eq. (4.6) by their asymptotic values for $\widetilde{B} \to 0$ and expanding the actions of Eq. (4.5) up to first order in $\widetilde{B}$. This reproduces, as expected, the perturbative results of Bogachek *et al.* [15] and Reimann *et al.* [62].

The result for the shell structure (i. e. the coarse-grained level density) in comparison to the exact quantum mechanical result is displayed in Fig. 4.8. For $R_c > R$, the agreement

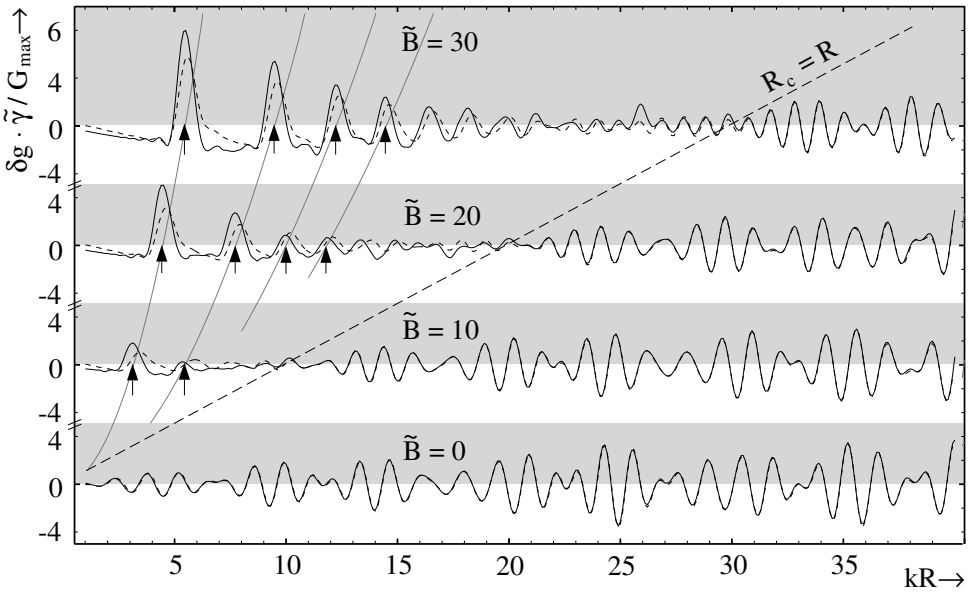


Figure 4.8: *The semiclassical level density of the disk billiard (solid) compared to the equivalently smoothed quantum-mechanical result (dashed). The smoothing width is $\tilde{\gamma} = 0.35$. Gray lines and the arrows indicate the positions of the first four Landau levels. In weak fields ($R_c > R$) the semiclassical result is in excellent agreement with the exact solution, for strong fields ($R_c \lesssim R$) the agreement is not satisfactory.*

with the exact quantum mechanical result is excellent. In the strong-field regime $R_C \lesssim R$, however, the agreement is not satisfactory. The positions of the Landau levels are reproduced, but their degeneracy is overestimated in the semiclassical approximation. In the extreme field limit ($R_c \ll R$) the Landau states dominate the level density. In this regime the cyclotron orbits dominate, since their degeneracy prefactor Eq. (4.10) grows linearly in $B$. As shown in Sec. 4.2.1.3, the cyclotron orbits can be analytically transformed to a harmonic oscillator. Thus, the semiclassical description of these orbits is *exact*. For extremely strong fields, the trace formula is therefore again a good approximation.

The same results have also been obtained for the full quantization of the system [1, 4]. To summarize, both the shell structure and the full quantization, in weak as well as in extremely strong fields, are well approximated by the semiclassical method. The regime $R_c \lesssim R$, however, is poorly reproduced by the trace formula.

## 4.3 Beyond the leading order: $\hbar$ corrections

### 4.3.1 The inherent $\hbar$ problem in the disk billiard

As explained in the previous section, a new class of periodic orbits appears in strong magnetic fields. These are the cyclotron orbits, which exist only for $\widetilde{B} > kR$. Whereas the bouncing orbits have a one-dimensional rotational symmetry, the cyclotron orbits are two-dimensionally translationally degenerate. The application of Creagh's trace formula Eq. (2.15) leads to contributions in $\hbar^{-3/2}$ stemming from the bouncing orbits. The cyclotron orbits, however, have a prefactor $\hbar^{-2}$ . Even though the trace formula is derived as the leading-order contribution in $\hbar$, its application to the disk billiard results in terms of different orders in $\hbar$.

The inherent $\hbar$ problem of the disk billiard is that these different powers in $\hbar$ are indeed necessary to describe the level density of the system. The leading order in $\hbar$ is given by the contributions of the cyclotron orbits. These describe the Landau levels correctly, which dominate the level density in the extreme strong field limit. At weak fields, however, $R_c > R$ and the trace formula only consists of the bouncing orbits.

In the two limits where one order in $\hbar$ is dominant, i. e. the extreme and the weak field limit, the trace formula was seen to be a good approximation. In the strong field regime ($R_c \lesssim R$) different powers in $\hbar$ become relevant, and the semiclassical description is not satisfactory (cf. Fig. 4.8). This observation is surprising, since the transition between the limiting cases is mainly governed by the smoothly varying degeneracy prefactor of the cyclotron orbits. The origin of the discrepancy between the semiclassical and the quantum result in the strong field regime needs further investigation.

Formally, the bouncing orbits give rise to an $\hbar$ correction in this regime – but, as we have just seen, they cannot be neglected. This naturally rises the question whether other $\hbar$ corrections are also relevant for the semiclassical description of this system. The following sections select various $\hbar$ corrections from physical and mathematical arguments and examine their influence. These investigations will finally show that all relevant effects can be described in a simple, intuitive picture. More mathematically motivated corrections will be of negligible influence. This is very convenient from an applicant's point of view, since the necessary modifications to the trace formula remain simple, and more involved $\hbar$ corrections are irrelevant for practical applications. A theorist, however, might be disappointed by the fact that all the elaborate lengthy formulas have so little influence in the end.

### 4.3.2 Reflection phases

The calculation of corrections to the Maslov index is motivated by two observations: First, a close look at the shell structure in Fig. 4.8 as well as at the corresponding full quantization data shows that the semiclassical approximation overestimates the degeneracy of the Landau levels, and completely misses the levels slightly higher in energy. A simple hand-waving argument links this behavior to a boundary effect: Quantum mechanically, a particle moving on a cyclotron orbit will feel the boundary even if classically not touching it. Particles on cyclotron orbits close to the boundary thus feel an additional confinement. This restriction to a smaller volume will lead to a higher energy. In this picture, not all the cyclotron orbits are degenerate. The orbits close to the boundary no longer have the

energy of the Landau level, but a slightly higher one. This corrects the observed defects of the semiclassical approximation. The boundary properties enter the standard trace formula only via the Maslov index, so that a correction of $\mu$ is indicated.

The second observation motivating a closer examination of the Maslov index can be illustrated with the diameter orbit. It exists only in the weak-field regime and develops into a cyclotron orbit at $R_c = R$. The action and the period change smoothly over this point, but the Maslov index does not: It is 4 for the bouncing, and 2 for the cyclotron orbit. A correction to the Maslov index should remove this spurious jump.

In my Diploma thesis [1], I suggested an $\hbar$-correction to the Maslov index, i. e. replacing it with a more sophisticated quantity explicitly depending on $\hbar$. This section will summarize the ansatz together with the main results.

#### 4.3.2.1 The Maslov index

The origin of the Maslov index can most easily be understood in the one-dimensional case. As presented in more detail in Sec. 2.1, the semiclassical approach approximates the wave functions by plane waves with the local wave number $k(x) = \sqrt{2m[E - V(x)]}$. This approximation obviously breaks down at the classical turning points where $E = V(x)$, so that the wavelength diverges. Expanding the wave function around the classical turning points and matching them to the plane-wave solutions far from the turning points leads to additional phases in the semiclassical quantization. In the limit $\hbar \to 0$ these are independent of the detailed shape of the potential. Each reflection at a soft[3] turning point gives a phase of $-\pi/2$, whereas each reflection at an infinitely steep wall gives a phase of $-\pi$. These phases (in units of $\pi/2$) are the Maslov indices.

In the case of the disk billiard, the Maslov index can be obtained by counting the classical turning points of the one-dimensional effective potential in the radial variable $r$. For skipping orbits, the Maslov index per bounce is 3, including one soft reflection at the centrifugal barrier and one hard-wall reflection. For the cyclotron orbits, the effective potential is a one-dimensional harmonic oscillator (see Sec. 4.2.1.3) with two soft turning points, and thus their Maslov index per period is 2. In higher dimensions, the Maslov index is less accessible to intuition. It can be described as a topological index characteristic for an orbit. Its calculation for two-dimensional systems is described in appendix A.2.3. For higher dimensions see e. g. Refs. [22, 66].

#### 4.3.2.2 Reflection phases

For finite $\hbar$ the additional phases stemming from classical turning points depend on the shape of the potential. This can be easily understood considering a cyclotron orbit at a distance $x_w$ from the billiard boundary. Neglecting the curvature of the boundary (which corresponds to the strong-field limit), the motion in the presence of the wall can be reduced to an effective 1D motion just as presented in Sec. 4.2.1.3. This is shown in Fig. 4.9. The upper row of diagrams shows the 2D motion, the lower row gives the reduction to the one-dimensional motion in an effective potential. Figure 4.9 (a) shows the unbounded case, in (b) the orbit is near the boundary, and (c, d) illustrate skipping orbits.

[3] In this context "soft" means that the slopes of the potential at the classical turning points are finite.

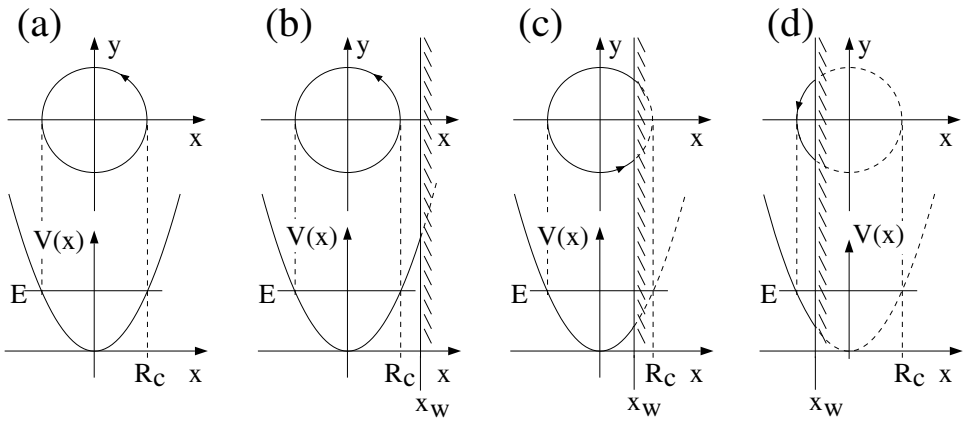


Figure 4.9: *The cyclotron orbit is equivalent to the motion in a one-dimensional harmonic oscillator (a). Neglecting its curvature, the billiard boundary can be implemented in the effective one-dimensional motion (b)-(d).*

A particle in the potential sketched in Fig. 4.9(b) is classically not influenced by the additional wall, since it will never touch it. Quantum mechanically, however, the wave function enters the classically forbidden region and thus feels the boundary even for $x_\mathrm{w} > R_c$. This leads to a smooth transition of the quantum-mechanical reflection phase $\varphi_R$ over $x_\mathrm{w} = R_c$. The semiclassical Maslov phase, in contrast, is discontinuous at this point. As explained in Sec. 4.3.2.1 above, it is $-\pi$ for $x_\mathrm{w} > R_c$ and $-3/2\pi$ for $x_\mathrm{w} < R_c$. The quantum mechanical boundary effects can be implemented in the semiclassical trace formula by replacing $\mu\pi/2$ by the reflection phase $\varphi_R$ of the corresponding one-dimensional motion. This smooth version of the Maslov phase will also remove the former clear separation between cyclotron orbits and skipping orbits. These two limiting cases are now continuously linked, with $\varphi_R$ ranging between $-\pi$ and $-3\pi/2$. We will refer to the orbits in the transition region, which are close to the boundary within $\hbar$, as to the *grazing orbits*.

In this approximation the calculation of the reflection phases is reduced to the problem of the one-dimensional harmonic oscillator in an additional square-well potential. The approach chosen in my Diploma thesis [1] was to integrate the quantum-mechanical problem numerically and calculate the reflection phases $\varphi_R$ from the solutions. Alternatively to this numerical approach, an analytical approximation of the reflection phase is possible. For a linear potential, the Schrödinger equation can be solved analytically. Matching the solutions with the boundary condition yields an expression of the reflection phases in terms of Airy functions:

$$\varphi_R = \begin{cases} -2\left(\frac{\pi}{4} + \arctan\left[\frac{A_i(X)}{B_i(X)}\right]\right) & \text{for } X \geq 0 \\ -2\left(\frac{\pi}{4} + \arctan\left[\frac{A_i(-X)}{B_i(-X)}\right] - \frac{2}{3}|X|^{2/3}\right) & \text{for } X < 0\ . \end{cases} \tag{4.15}$$

Expanding the potential at the turning point to linear order, these reflection phases can be used for arbitrary potential shapes. In this approximation, $X$ is given by

$$X = \left(\frac{3}{2}\int_T^W \sqrt{|E - V(x)|}\, dx\right)^{2/3}\ , \tag{4.16}$$

with the classical turning point $T$ and the position of the hard wall $W$. For the harmonic oscillator considered above, one finds explicitly

$$X = \begin{cases} \left[\frac{3}{4}\sqrt{\widetilde{E}}\left( \quad \widetilde{x}_{\rm w}\sqrt{\widetilde{x}_{\rm w}^2-1} - \operatorname{arcosh}(\widetilde{x}_{\rm w})\right)\right]^{(2/3)} & \text{for } |\widetilde{x}_{\rm w}| \geq 1 \\ -\left[\frac{3}{4}\sqrt{\widetilde{E}}\left(\frac{\pi}{2} - |\widetilde{x}_{\rm w}|\sqrt{\widetilde{x}_{\rm w}^2-1} - \arcsin(|\widetilde{x}_{\rm w}|)\right)\right]^{(2/3)} & \text{for } |\widetilde{x}_{\rm w}| < 1\ , \end{cases} \tag{4.17}$$

where $\widetilde{x}_{\rm w} := x_{\rm w}/R_c$. An equivalent approach to the reflection phase was used in a different context by Isihara and Ebina [44].

The corrections to the Maslov index obtained from the numerical approach and the analytic approximation of the reflection phase are equivalent within the context of this work. Fig. 4.10 shows the result of the quantum mechanical calculation for the reflection phase $\varphi_R$. As expected, the transition from $-\pi$ at $x_{\rm w} \gg R_c$ to $-3/2\pi$ at $x_{\rm w} \ll R_c$ is smooth. The transition gets sharper if $(kR)^2/\widetilde{B}$ increases. For $(kR)^2/\widetilde{B} \to \infty$, which corresponds to the semiclassical limit $\hbar \to 0$, the standard Maslov phase (thick line) is reproduced. Fig. 4.10 shows that quantum corrections have the greatest influence on the grazing orbits ($x_{\rm w} \approx R_c$) and on orbits with $x_{\rm w} \gtrsim -R_c$. The latter are known as the *whispering gallery* orbits, as they move in a narrow region along the boundary.

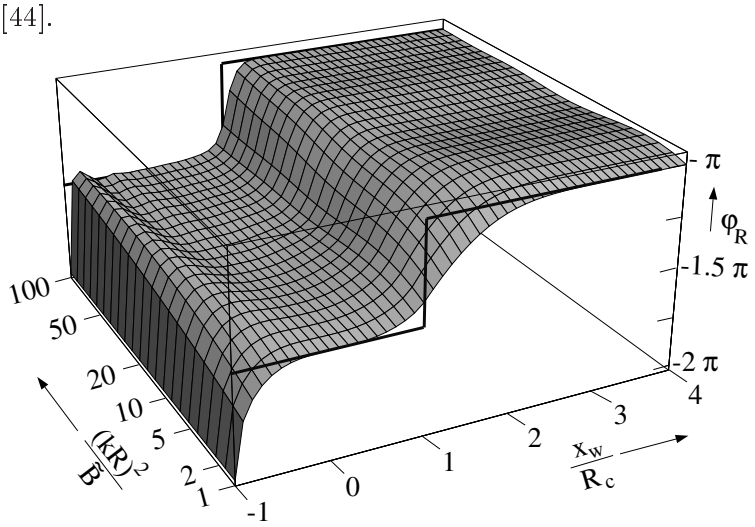


Figure 4.10: *The reflection phase $\varphi_R$ in dependence of the distance of the center of gyration from the boundary $x_{\rm w}$. The transition from $x_{\rm w} < R_c$ to $x_{\rm w} > R_c$ is continuous and gets sharper for increasing $(kR)^2/\widetilde{B}$. In the limit $(kR)^2/\widetilde{B} \to \infty$, which corresponds to the semiclassical limit $\hbar \to 0$, the Maslov phase (thick line) is recovered.*

#### 4.3.2.3 Comparison to the quantum-mechanical result

Fig. 4.11 depicts the semiclassical shell structure calculated with reflection phases in the whole range from zero field to full Landau quantization (solid). The comparison with the exact quantum result (dashed) shows that the semiclassical approximation is now valid for arbitrarily strong fields, in contrast to the standard trace formula result displayed in Fig. 4.8. Especially the degeneracies of the Landau levels are now reproduced correctly. This shows that the replacement of the Maslov index by the reflection phase is an important correction in the intermediate strong field regime. The reflection phase explicitly depends on $\hbar$, so that the inclusion of this term formally corresponds to a correction in higher than leading order in $\hbar$.

Some bifurcations of important orbits are marked with vertical lines in Fig. 4.11. The quality of the semiclassical approximation is excellent even at these points, where the semiclassical trace formula is expected to diverge. This apparent contradiction will be explained in the following section. There, the bifurcations will be included in the trace

formula, and the influence of the corresponding $\hbar$ correction will be analyzed for the various field regimes.

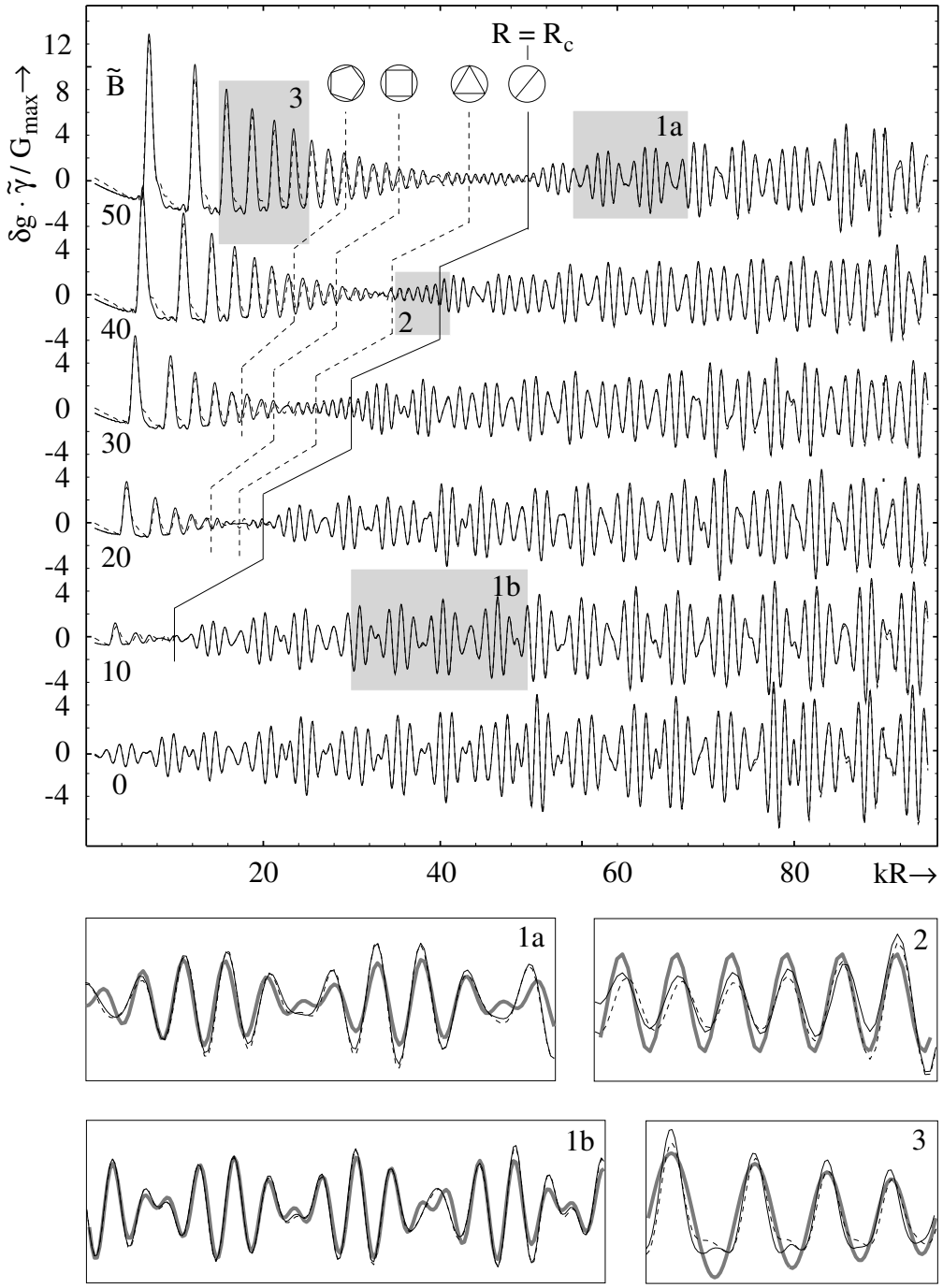


Figure 4.11: *The semiclassical coarse-grained ($\widetilde{\gamma} \approx 0.35$) level density of the disk billiard with corrected reflection phases (solid) compared to the equivalently smoothed quantum-mechanical result (dashed). The agreement is excellent in the whole range of energies, disk radii, and magnetic fields. The vertical lines indicate the bifurcation points of the most important orbits. The shaded regions are enlarged in the figures below. The thick gray lines correspond to the interpretation of the level density as given in Sec. 4.4.*

### 4.3.3 Bifurcations

In the disk billiard, the orbits $(v,w)^{\pm}$ vanish pairwise with increasing magnetic field (or decreasing energy) in *tangent bifurcations* (see Fig. 4.4). This type of bifurcation was already introduced in Sec. 2.4. Due to the continuous symmetry of the disk billiard, the integration considered there has to be performed over the angular momentum $L$ instead of $r$, but apart from that the schematic behavior of Fig. 2.1 is directly recovered. Fig. 4.12 shows the situation for the triangular[4] orbits. The stationary points of $S(L)$ in the first row correspond to the periodic orbits plotted below. Fig. 4.12(A) shows the generic

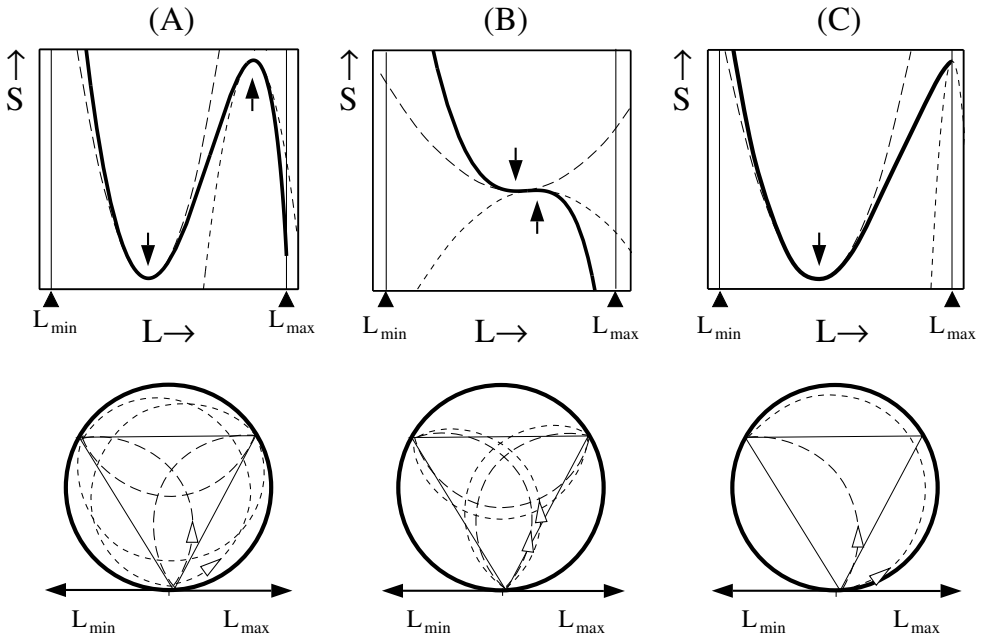


Figure 4.12: *$\hbar$ corrections to the stationary phase approximation of the trace integral of the level density. Upper row: Classical action $S$ in dependence of the angular momentum $L$ (solid). Dashed lines give the quadratic approximations at the stationary points (arrows). Lower row: Classical orbits corresponding to the stationary points of $S(L)$. (A) Generic Gutzwiller case, (B) close to a bifurcation, (C) close to the integration limit: creeping orbits.*

situation, where the stationary points are well separated from each other and from the integration limits. There, the stationary phase approximation according to Eq. (2.9) is well justified. Near a bifurcation, the stationary points are in close proximity. This is shown in Fig. 4.12(B). The situation corresponds exactly to the one discussed in Sec. 2.4. There is was outlined that uniform approximations are the appropriate tool to overcome the spurious divergencies of the standard Gutzwiller approach at the bifurcation points.

Applying the uniform approximation for tangent bifurcations Eqs. (B.7, B.8) to the disk billiard, a modified trace formula which incorporates all bifurcations can be derived. This trace formula reads

$$\delta g = \frac{1}{\pi\hbar} \sum_{\beta=(v,w)} D_\beta [a\mathrm{Ai}(\eta)\cos(\chi) + b\mathrm{Ai}'(\eta)\sin(\chi)] \,. \tag{4.18}$$

[4]Note that $S(L) = S(L,\beta)$, i. e. the functional dependence of $S$ on $L$, depends on the type of orbit.

with

$$
\begin{aligned}
D_\beta &= \frac{1}{E_0}\frac{\pi}{\sqrt{kR}}\cos\Theta\sqrt{\frac{R_c\sin\Theta}{vs}} \\
a &= \left(\frac{3}{2}v\left|\frac{R_c}{R}\widetilde{\gamma}-\frac{s\sin\Theta}{R_c}\right|+\frac{3\pi(\sigma_{\beta^+}-\sigma_{\beta^-})}{8}\right)^{1/6} \\
b &= \frac{1}{a}\left(\frac{s}{R\cos(\Theta)}-\frac{2\widetilde{\gamma}}{\pi}\right) \\
\eta &= \begin{cases} +a^4 & \text{for} \quad \sin\Theta > R_c/R \\ -a^4 & \text{else} \end{cases} \\
\chi &= v\left(\frac{R_c}{R}\frac{\pi}{2}+\frac{R}{R_c}\frac{\sin(2\Theta)}{2}\right)+\frac{\pi(\sigma_\beta^+ + \sigma_\beta^-)}{4} \\
\widetilde{\gamma} &= \begin{cases} \mathrm{acos}(R\sin(\Theta)/R_c) & \text{for } \sin\Theta > R_c/R \\ \mathrm{acosh}(R\sin(\Theta)/R_c) & \text{else} \end{cases} .
\end{aligned}
$$

For the reasons mentioned in Sec. 3.4, again the smoothed level density is considered in the numerical evaluation. The implementation of the smoothing in the trace formula requires special care, as the amplitude factors of Eq. (4.18) are oscillating functions. The procedure how to deal with this complication is discussed in Sec. 3.3.1. The result of the uniform approximation, together with the influence of the smoothing scheme, is examined in Fig. 4.13. There the contributions of the $\beta = (4,1)^{\pm}$ orbits to the oscillating part of

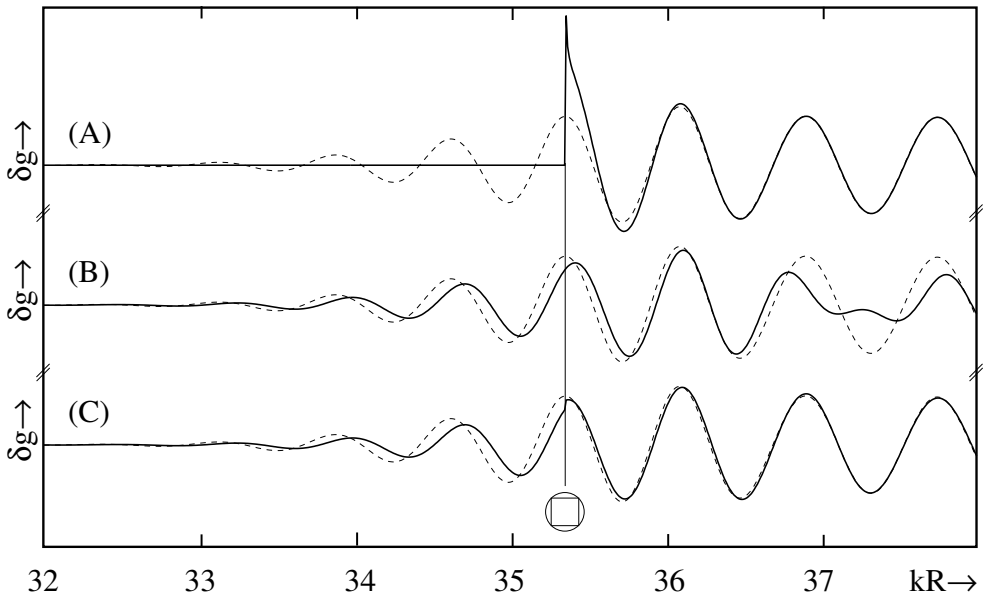


Figure 4.13: *The influence of the smoothing scheme on the uniform approximation. All data correspond to the contributions of the $\beta = (4,1)^{\pm}$ orbits to the semiclassical level density for $\widetilde{B} = 50$ and $\widetilde{\gamma} \approx 0.21$. The dashed lines in (A-C) give the uniform result together with the exact implementation of smoothing according to Sec. 3.3.1. The solid lines show (A) Gutzwiller result; (B) naive implementation of the smoothing, assuming slowly varying amplitudes; (C) improved ansatz as explained in the main text.*

the level density are plotted for $\widetilde{B} = 50$ and $\tilde{\gamma} \approx 0.21$. In Fig. 4.13(A), the solid line gives the result of the Gutzwiller trace formula, with smoothing according to Eq. (3.14). The

characteristic divergence at the bifurcation point can clearly be seen. For $\widetilde{B} \lesssim 35.36$ the $(4,1)^{\pm}$ orbits classically do no longer exist, so that their contribution to the Gutzwiller trace formula is zero. The uniform approximation Eq. (4.18) with smoothing according to Eq. (3.29) is illustrated by the dashed lines in (A-C). This ansatz interpolates smoothly over the bifurcation. Far on the *real side* of the bifurcation, i. e. the side where the orbits classically exist, the uniform approximation reproduces, as expected, the Gutzwiller result. On the *complex side*, the uniform approximation includes contributions of ghost orbits. These are damped exponentially. The detailed discussion of the effects of the bifurcations on the level density is postponed until the influence of the smoothing scheme on the uniform result is examined.

In (B), the correct smoothing scheme (dashed) is compared to the naive application of Eq. (3.14). This ansatz corresponds to the approximation of the Airy functions in Eq. (4.18) as constants. Except for the vicinity of the bifurcation, this approach fails completely. This is easily understood looking at the formula for the uniform treatment of the tangent bifurcation Eqs. (B.7, B.8). Applying the smoothing scheme of Eq. (3.14) to this expression, the damping depends on the average $\partial S/\partial E$ of the two orbits. This does not converge to the correct limit far from the bifurcation, which is given by the Gutzwiller expression. There the damping is given in terms of the individual orbit frequencies. The correct asymptotic behavior on the real side can be imposed by interpreting the damping terms as parts of the semiclassical amplitudes, thus including them in the sum and difference terms of the amplitudes in Eqs. (B.7, B.8). This approach, however, is restricted to the real side, since on the complex side the actions are imaginary. This results in complex arguments for the window function, which is not covered by the smoothing scheme of Sec. 3.2. In Fig. 4.13(C), this modified smoothing scheme (solid) is compared with the exact implementation according to Eq. (3.29) (dashed). On the real side this simple approach leads to acceptable results. The difference to the exact inclusion of smoothing on the complex side of the bifurcation, however, is not negligible.
In conclusion, Fig. 4.13 shows that the correct implementation of smoothing is crucial when considering bifurcations in the trace formula. It leads to significant corrections to the standard schemes.

Now as the effect of the smoothing scheme has been examined, the influence of the bifurcations on the level density should be considered. In Fig. 4.14(A), once again the contribution of the $(4,1)^{\pm}$ orbits to the level density with (dashed) and without (solid) uniform approximation is plotted. The large mismatch confirms that neglecting the bifurcation results in a wrong contribution of a single orbit to the trace formula. The total level density, however, is not much affected. This is shown in (B, D) for two smoothing widths. Broad smoothing leads to a small number of orbits which contribute to the trace sum. Since the bifurcation points of these orbits do not coincide, the other orbits partially mask the effect of a bifurcation (B). For narrow smoothing (D) more orbits contribute to the trace formula, and the net effect of the bifurcations further decreases. Even the widths of the poles at the divergencies get less wide when more orbits are included. This effect is due to higher repetitions of the bifurcating orbits. These bifurcate at the same points as the primitive orbits. Fig. 4.14 indicates that the effects of the different bifurcations compensate to a great extent.

Although a finer resolution leads to a larger number of bifurcations included in the trace formula (illustrated by vertical lines in Fig. 4.14(C)), their net effect decreases. The shell structure is therefore more affected by the $\hbar$ corrections than the full quantization data. For extremely broad smoothing, however, the effect of the bifurcations also decreases. This

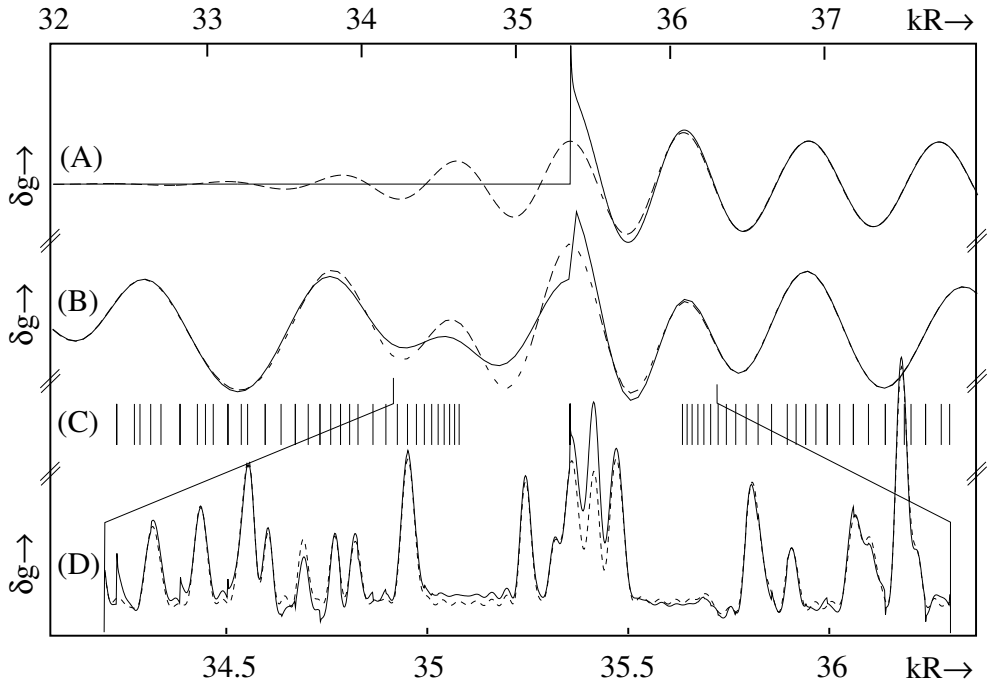


Figure 4.14: *Comparison between the standard trace formula (solid) and the uniform approximation (dashed) for* $\widetilde{B} = 50$. *(A) shows the contribution of the orbits* $(4,1)^{\pm}$, *(B) and (D) give the level density with smoothing widths of* $\widetilde{\gamma} \approx 0.21$ *and* $0.012$ *in* $kR$. *The vertical lines (C) indicate the positions of the bifurcations of the orbits included in the calculation of (D).*

is due to the properties of the periodic orbits in the disk billiard: At the bifurcation point, the quasiperiod (i. e. the geometrical orbit length) is given by (cf. Eq. (4.14))

$$L_{\mathrm{bif}} = Rv\pi \sin(\pi w/v) \approx R\pi^2 \ . \tag{4.19}$$

The approximation on the r.h.s. is justified for all orbits except the diameter (where $L_{\mathrm{bif}} = 2R\pi$), since for strong smoothing only the orbits with $w = 1$ are relevant. Smoothing widths equivalent to an cut-off length $L_{\max} \approx R\pi^2 w$ therefore lead to a strong damping of the contributions from bifurcations. A cut-off length $L_{\max} < R\pi^2 w$ suppresses the bifurcations completely.[5] This is the reason why in Fig. 4.11 the expected divergencies at the bifurcations can not be seen.

The maximum effect of the bifurcations on the level density should therefore be observed for medium strong smoothing. This situation is plotted in Fig. 4.15, where the length cutoff of the triangular window function was taken to be $L_{\max} = 12R$, corresponding to a smoothing width of $\widetilde{\gamma} \approx 0.195$. The dashed lines give, just as in Fig. 4.11, the exact quantum result with equivalent smoothing. It is compared to the standard Gutzwiller approach in (A, C) and to the uniform approximation in (B, D). Even for this situation, where the influence of the bifurcations is maximal, the uniform approximation only leads to marginally better results than the standard trace formula.

In conclusion, the influence of the bifurcations is negligible for all spectral resolutions from the shell structure up to full quantization. Fig. 4.11 illustrates that the contributions are

[5] This strictly holds only for window functions with $F(L) = 0 \ \forall \ L > L_{\max}$, as for the triangular window function used here.

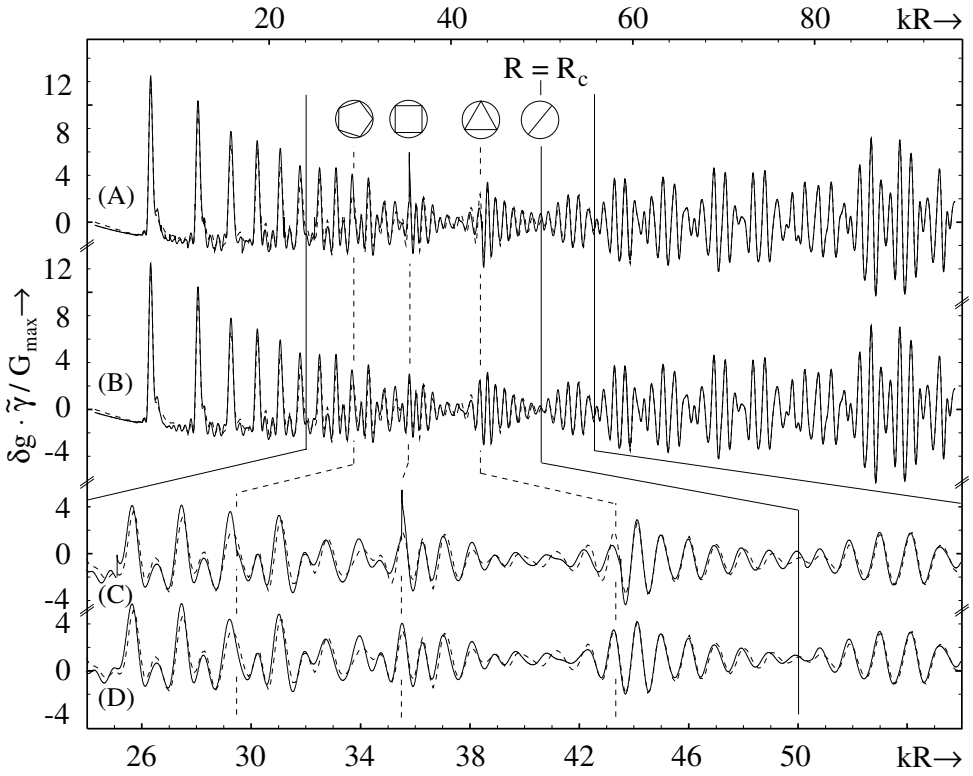


Figure 4.15: *The influence of the bifurcations. Dashed: exact quantum result for* $\widetilde{B} = 50$, $\widetilde{\gamma} \approx 0.195$. *Solid lines correspond to the standard Gutzwiller formula in (A, C) and to the uniform approximation in (B, D). The* $\hbar$ *correction from the bifurcations is small and strongly localized at the bifurcation points.*

damped out for large smoothing. For intermediate strong smoothing, as presented in Fig. 4.15, the uniform approximation slightly improves the semiclassical level density. The effect, however, is localized in a narrow region around the bifurcations and hardly relevant in size. For higher resolution spectra, Fig. 4.13 shows that the contributions of the bifurcations mostly cancel. The widths of the divergencies are becoming smaller, and their net effect further decreases. The bifurcations therefore do not give rise to a relevant $\hbar$ correction of the semiclassical level density, even though they lead to divergencies of the trace formula. It should be noted that the $\hbar$ correction from the bifurcations is comparable in size with the correction stemming from the correct implementation of smoothing. It is therefore not reasonable to include the uniform approximation without adapting the smoothing scheme.

### 4.3.4 Grazing

The mechanism which necessitated the implementation of the uniform approximation in the last section was that the final stationary phase approximation in the derivation of the trace formula for the disk billiard failed close to bifurcations points. Fig. 4.12, which plots the dependence of the action $S$ on the angular momentum $L$ of the triangular orbit, shows that another correction might be relevant in this step.

In Fig. 4.12(A) the stationary points, which correspond to the periodic orbits sketched below, are well separated both from each other and from the integration limits. Fig. 4.12(C) illustrates the case where the $\beta^+$ orbit approaches the maximum angular momentum. For

orbits which creep along the billiard boundary, one integration limit coincides with the stationary point. The contributions of these paths to the trace sum are expected to be half the value of the original formula. These corrections apply for orbits close to the boundary, so that they are called *grazing corrections*. At $\widetilde{B} = kR$, i. e. for $R_c = R$, this correction applies to all $\beta^+$ orbits simultaneously[6]. For this magnetic field strength the effect should therefore be most pronounced.

The grazing correction can be included in the trace formula by incorporating the finite integration limits. This leads to Fresnel type of integral instead of the Gaussian integrals occurring for the unconstraint integration according to Eq. (2.9). The corresponding modification of the trace formula for the disk billiard reads

$$\delta g = \frac{1}{\pi\hbar}\mathcal{I}m\left[\sum_{\beta} A_\beta B_\beta e^{i\left(\frac{S_\beta}{\hbar}-\mu_\beta\frac{\pi}{2}\right)}\right] . \tag{4.20}$$

The only changes to the original expression are the factors $B_\beta$, which replace the additional phases $\delta$ in Eq. (2.15). These complex factors are defined as

$$B_\beta = \sum_{\xi=\xi_u,\xi_o} 2^{-1/2}\left[C(\xi) + i\alpha S(\xi)\right] . \tag{4.21}$$

For $\beta^+$ orbits and $R_c < R$ the coefficient $\alpha = -1$, otherwise $\alpha = +1$. The $\xi_{\substack{u\\l}}$ are determined by the upper and lower integration limit, respectively:

$$\xi_{\substack{u\\l}} = \sqrt{\frac{kR}{\pi}}\sqrt{\frac{2vs}{R_c\sin\Theta}}\left|\frac{R_c \mp R}{s - \zeta R\cos\Theta} \mp \zeta\cos\Theta\right| . \tag{4.22}$$

The geometrical quantities $\Theta$ and $s$ are explicitly given in Eq. (4.7) on page 32. $\zeta = +1$ for the $\beta^+$, and $\zeta = -1$ for the $\beta^-$ orbits. For constant energy $\xi$ is proportional to $\hbar^{-1/2}$. Taking into account the finite integration limits therefore leads to corrections of the order $\sqrt{\hbar}$ beyond the leading order.

The numerical evaluation of the trace formula again forces the introduction of a finite smoothing width. The Fresnel integrals $C$ and $S$ are oscillating functions. Therefore the common damping ansatz Eq. 3.18 can not be used. The appropriate generalization is given in Sec. 3.3.1, and Eq. (3.29) applies to the situation considered here. Fig. 4.16 shows the semiclassical level density with (solid black) and without (gray) grazing correction. The simple smoothing which assumes the Fresnel factor to be a slowly varying function is given by the dotted line. The magnetic field is $\widetilde{B} = 50$, so that $R_c = R$ for $kR = 50$. The smoothing width is $\widetilde{\gamma} \approx 0.33$. The upper part of the figure shows the contributions of the $\beta^+$ orbits. The closeup in the inset confirms that the simple smoothing (dashed) leads, indeed, to a 50% correction of the Gutzwiller contribution (gray) of the $\beta^+$ orbits. Including the correct windowing (solid black), however, mostly compensates this effect. Even more surprising is the behavior of the $\beta^-$ orbits. Although they are not as close to the integration limit as the $\beta^+$ orbits, their grazing correction is nearly of the same magnitude. The lower part of the diagram shows the total effect of the grazing correction including all orbits. At $\widetilde{B} = 50$, which corresponds to $R_c = R$ where the grazing effect was expected to be most pronounced, the influence of the correction is small. The main

[6]For $R_c = R$ all $\beta^+$ orbits coincide, building the *whispering gallery*.

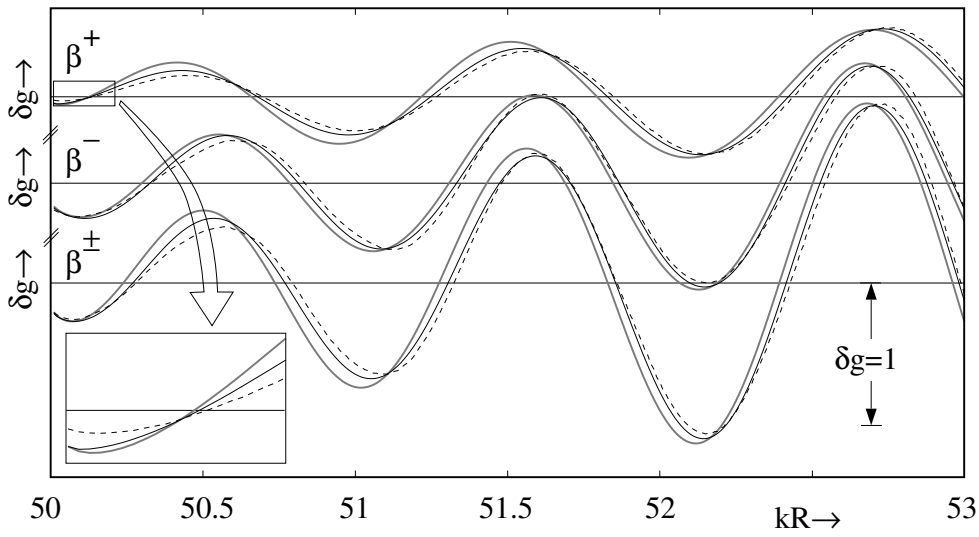


Figure 4.16: *The effect of the grazing correction for* $\widetilde{B} = 50$ *and* $\widetilde{\gamma} \approx 0.33$. *Gray: without grazing correction; dashed: grazing correction with simple smoothing; solid black: grazing correction with correct smoothing. Offset for clarity.*

effect is not a variation of the amplitude, but a slight shift of the phase stemming from the complex part of $B_\beta$.

This result shows that the $\hbar$ correction stemming from grazing can be neglected in the trace formula of the disk billiard. Please note that the effect of the correct windowing is of the same order of magnitude as the correct implementation of the grazing effect. As for the bifurcation treatment above, this again shows that the technical detail of the implementation of smoothing is of considerable importance.

## 4.4 Semiclassical interpretation of $\delta g$

An attractive feature of the semiclassical approximation which was not used until now is the simple, intuitive picture it gives. This should be exploited in the following to explain the shell structure of the disk billiard in terms of classical quantities.

According to the trace formula Eq. (2.15), each periodic orbit $\beta$ contributes an oscillating term to $\delta g$. Its frequency is determined by the classical action $S_\beta$ along this path, which can be locally approximated by

$$S_\beta(k) = S_\beta(k_0) + \hbar\, G_\beta(k)\ (k - k_0)\ , \tag{4.23}$$

with the *quasiperiod* $\hbar G$. For billiard systems the quasiperiod is, according to Eq. (3.21), identical to the geometrical orbit length $L$ given in Eq. (4.14). The amplitudes of the oscillating terms are $A_\beta\, F(G_\beta)$, where $F$ is the window function that depends on the desired smoothing of the level density. Prior to the interpretation of the contributions of the various orbits to $\delta g$, the behavior of $G_\beta (= L_\beta)$ and $A_\beta$ shall be discussed.

Fig. 4.17 shows the dependence of $G$ on the ratio $R_c/R = kR/\widetilde{B}$. Note that for $R_c > R$ (see right diagram of Fig. 4.17) $G$ is independent of the direction of motion $\pm$, even if the classical action depends on it. In strong fields ($R_c < R$, left diagram) $G$ is different for the "+" and the "–" orbits. Only at the bifurcation points, where the two orbits coincide,

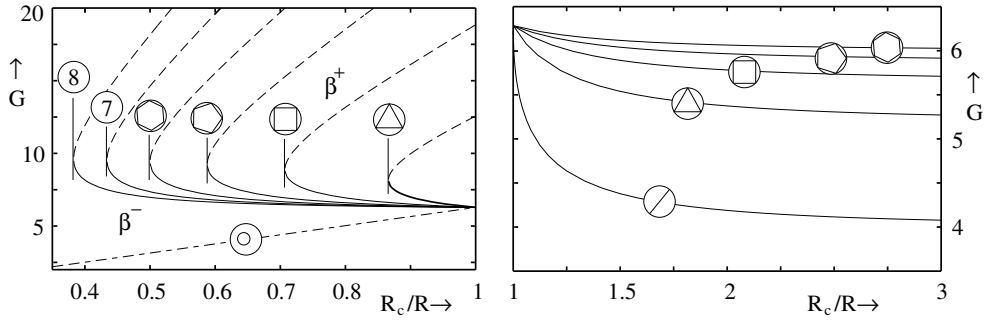


Figure 4.17: *The quasiperiods $G$ of the most important orbits in dependence of $R_c/R$. For $R_c > R$, $G$ is independent of the index $\pm$. The orbit bifurcation points in strong fields (vertical lines) can clearly be seen.*

they have identical $G$. According to Eq. (4.19), the value of $G$ at the bifurcation points converges to $w \cdot \pi^2 R$ for strong fields.

In Fig. 4.18 the amplitudes of the orbits relative to the $B = 0$ values,

$$A_\beta^0 = \frac{\sin^{3/2}\Theta}{\sqrt{v}} \,, \tag{4.24}$$

are plotted versus the ratio $R_c/R$. The amplitude of the "–" orbit is always larger than that of the corresponding "+" orbit. At $R_c = R$, where the "+" orbits change the topology (see Fig. 4.3), their amplitudes are zero, so that these discontinuities do not lead to artefacts in the level density. At the tangent bifurcations discussed above, the orbit amplitudes diverge.

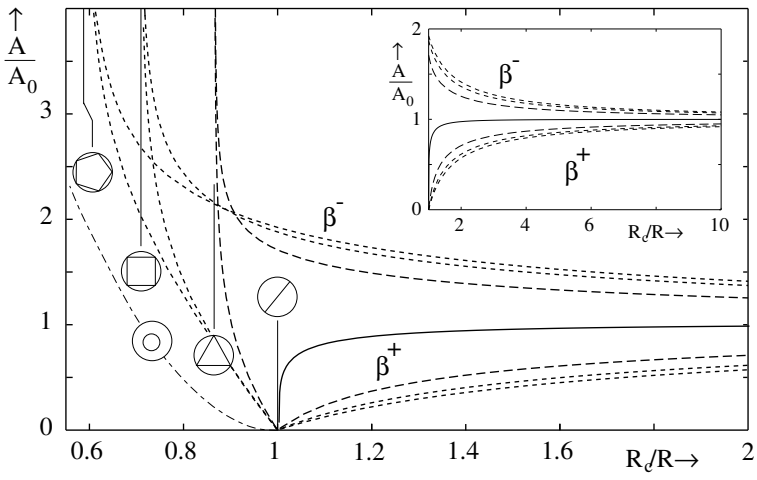


Figure 4.18: *The amplitudes of the dominating orbits $\beta = (v,1)^{\pm}$ with $v = 2,\ldots,5$ relative to their $B = 0$ value. (The amplitude of the cyclotron orbit is in arbitrary units.) At the bifurcation points $R_c = \sin(\pi\ v/w)$ indicated by vertical lines, the amplitudes diverge. For $R_c > R$ the amplitudes of the bouncing orbits quickly approach their asymptotic (zero-field) value. The inset shows this convergence in a wider range.*

Now the shell structure shall be interpreted in these classical terms, starting with the weak-field regime ($R_c > R$). The amplitudes for zero field given in Eq. (4.24) are proportional to $v^{-1/2}$, favoring orbits with a small number of bounces $v$. The dependence of the amplitudes on the magnetic field as shown in Fig. 4.18 indicates that in the region where the "–" orbits differ significantly from the "+" orbits, the latter are negligible. These effects[7] together strongly favor the $(2,1)$ and the $(3,1)^-$ orbit. They end up with comparable amplitudes. From this picture a pronounced beating pattern from the interference of the diameter and the triangular orbit is expected as the dominating feature of the level density. This beating

[7] The $G$ dependence of $F(G)$ also slightly supports this effect.

pattern is indeed observed (cf. Fig. 4.11). The analogous effect in three dimensional metal clusters is known as *supershell oscillations* [61].[8] The semiclassical description furthermore predicts that this beating will persist in homogeneous magnetic fields up to a strength of $\widetilde{B} = kR$. This is in agreement with the findings in Fig. 4.11. The thick gray lines in the frames (1a) and (1b) correspond to a function[9]

$$\sin(kG_{(1,2)}) + \sin(kG_{(1,3)^-}) = \sin\left(k\frac{\Delta G}{2}\right)\ \sin\left(k\frac{\bar{G}}{2}\right)\ . \tag{4.25}$$

It correctly predicts the structure of the level density in this regime.

Approaching the field strength where $R_c = R$, all orbits change $G$ sharply to $2\pi R$. At this point, the $\beta^+$ orbits coincide. The amplitude of this collective mode is small. The $\beta^-$ orbits differ from each other at $R_c = R$. The change of $S$ with varying $B$ is, however, identical for all orbits, since according to Eq. (4.23) all bouncing orbits have the same lengths for $R_c = R$. This implies that the variation with magnetic field is coherent for all bouncing orbits, although their absolute values of $S$ are different. The semiclassical picture therefore predicts that the beating behavior will disappear at $R_c = R$, leaving just a simple oscillation with the common frequency. In Fig. 4.11 this sudden stop of the beat at $R_c = R$ can clearly be seen. The gray line in frame 2 shows that the frequency of the remaining single oscillation is predicted correctly.

In strong fields, only cyclotron orbits and bouncing orbits with a great number of bounces $v$ exist. The amplitudes of the latter are proportional to $v^{-1/2}$, so that in the strong field limit the cyclotron orbits are expected to dominate the level density. The gray lines in frame 3 of Fig. 4.11 show the corresponding oscillating term,[10] which, indeed, reproduces the main feature of the quantum-mechanical result (solid black). The skipping orbits with greatest amplitudes are those which are close to their bifurcation points. All those orbits have nearly the same value of $G = w \cdot \pi^2 R$. Their contributions should therefore interfere constructively, giving rise to small structures in the level density of this period. Such structures can indeed be observed in a higher-resolution spectrum, and their spacing is consistent with this simple picture.[11] The effect of the only relevant $\hbar$ contribution was already discussed in Sec. 4.3.2. The reflection phases remove the degeneracy of all cyclotron orbits, leading to slightly higher energies of the orbits close to the billiard boundary. This leads to a reduction of the Landau peak heights and to an increased level density slightly above the Landau levels. This correction is only relevant in the intermediate strong field regime $R_c \lesssim R$.

This analysis shows that the simple semiclassical picture using only the classical properties of three periodic orbits is able to explain the main features of the quite complicated behavior of the level density[12] for arbitrarily strong fields.

[8] In the 3D spherical cavity, the beat is due to the interference of the triangle and the square orbits (see Ref. [11]).

[9] The phases are, of course, adjusted.

[10] For a simpler comparison, the amplitude is chosen to rise quadratically, as indicated by Eq. (4.10).

[11] For details see Refs. [1, 4].

[12] Here the dependence of the level density on the energy was interpreted. For the dependence on the magnetic field a completely analogous approach is possible.

## 4.5 Summary

In this chapter, a semiclassical approximation for the level density of the disk billiard in homogeneous magnetic fields was derived. The agreement of the standard trace formula with the exact quantum result is excellent for small fields as well as for extremely strong fields, but not in the intermediate regime. This failure was suspected to be due to $\hbar$ corrections to the trace formula. Three different $\hbar$-corrections have been analyzed.

First a correction to the Maslov index was considered. This exhibits a discontinuity when the reflection at the hard boundary is, with increasing field strength, replaced by the soft turning point in the magnetic potential. A one-dimensional approximation leads to reflection phases which interpolate smoothly between these limits. It was shown that replacing the Maslov indices by reflection phases is of great importance in the strong field regime $R_c \lesssim R$. This holds for the shell structure as well as for full quantization.

At bifurcations, the second-order approximation of the action $S$ around stationary points breaks down, leading to spurious divergencies in the semiclassical amplitudes. A uniform approximation to higher order in $S$ shows that at the tangent bifurcation the contribution to the trace formula is increased by a factor $\hbar^{1/6}$ [70]. The inclusion of this $\hbar$ correction is important when one considers the contribution of individual orbits to the trace formula. The corrections, however, rapidly loose influence if either many orbits are included (which generally is the case if a higher resolution of the spectrum is required), or the smoothing is so broad as to suppress the bifurcating orbits strongly. The main result of this consideration is that the bifurcations have the maximum influence on moderately coarse-grained level densities. But even for this case, the $\hbar$ corrections due to the bifurcations are only marginal.

Finally the creeping correction, formally occurring due to finite integration limits, was shown to be completely negligible in the semiclassical approximation — although on first sight it is expected to be a 50% effect. Both the implementation of bifurcation and of grazing effects require a modification of the smoothing procedure. The corrections from the adapted smoothing are in both cases comparable to the magnitude of the $\hbar$ corrections themselves.

These considerations show that the only relevant correction to the trace formula is given by the reflection phases. Including this, the semiclassical trace formula for the level density is a good approximation for arbitrarily strong fields. It reproduces the exact quantum-mechanical result with a remarkably reduced numerical effort. For the quantum-mechanical calculation shown in Fig. 4.11, about 2500 eigenvalues had to be calculated and numerically smoothed for each value of $\widetilde{B}$, whereas the semiclassical result is obtained summing the contributions of just 20 orbits.[13]

The main features of the level density could be explained in a simple picture. The classical properties of three interfering orbits are sufficient to explain the behavior of the level density in arbitrary field strengths. In weak fields the diameter together with the the inwards-curved triangular orbit lead to a pronounced beating pattern. For $\widetilde{B} = kR$ all orbits interfere constructively, and in strong fields the cyclotron orbits dominate. They lead to the Landau quantization. The degeneracy of the Landau levels is reproduced correctly implementing the proximity effect of the boundary via the refection phase.

[13] For $R_c > R$ even 10 orbits are sufficient.